Published in final edited form as:

J Biomech. 2021 August 26; 125: 110543. doi:10.1016/j.jbiomech.2021.110543.

Mechanics of Ascending Aortas from TGFβ-1, -2, -3 Haploinsufficient Mice and Elastase-Induced Aortopathy

Brooks A Lane[a], **Mrinmay Chakrabarti**[b], **Jacopo Ferruzzi**[c], **Mohamad Azhar**[b,d], **John F Eberth**[a,b,*]

[a]Biomedical Engineering Program, University of South Carolina, Columbia, SC 29208 USA

[b]Cell Biology and Anatomy Department, University of South Carolina School of Medicine, Columbia, SC 29208, USA

[c]Department of Bioengineering, University of Texas at Dallas, Richardson, TX, 75080, USA

[d]William Jennings Bryan Dorn VA Medical Center, Columbia, SC 29209, USA

Abstract

Transforming growth factor-beta (TGFβ-1, -2, -3) ligands act through a common receptor complex yet each is expressed in a unique and overlapping fashion throughout development. TGFβ plays a role in extra-cellular matrix composition with mutations to genes encoding TGFβ and TGFβ signaling molecules contributing to diverse and deadly thoracic aortopathies common in Loeys-Dietz syndrome (LDS). In this investigation, we studied the TGFβ ligand-specific mechanical phenotype of ascending thoracic aortas (ATA) taken from 4-to-6 months-old *Tgfb1*$^{+/-}$, *Tgfb2*$^{+/-}$, and *Tgfb3*$^{+/-}$ mice, their wild-type (WT) controls, and an elastase infusion model representative of severe elastolysis. Heterozygous mice were studied at an age without dilation to elucidate potential pre-aortopathic mechanical cues. Our findings indicate that ATAs from *Tgfb2*$^{+/-}$ mice demonstrated significant wall thickening, a corresponding decrease in biaxial stress, decreased biaxial stiffness, and a decrease in stored energy. These results were unlike the pathological elastase model where decreases in biaxial stretch were found along with increases in diameter, biaxial stress, and biaxial stiffness. ATAs from *Tgfb1*$^{+/-}$ and *Tgfb3*$^{+/-}$, on the other hand, had few mechanical differences when compared to wild-type controls. Although aortopathy generally occurs later in development, our findings reveal that in 4-to-6 month-old animals, only *Tgfb2*$^{+/-}$ mice demonstrate a significant phenotype that fails to model ubiquitous elastolysis.

Keywords

Loeys-Dietz syndrome (LDS); connective tissue disorders; transforming growth factor-beta

---

[*]Corresponding author: John F. Eberth, Ph.D., john.eberth@uscmed.sc.edu, Address: USC SOM CBA, Bldg.1, Rm. C-36, Columbia, South Carolina, 29208.

Conflict of interest statement
The authors declare no financial or nonfinancial conflicts of interest.

1. Introduction

Transforming growth factor-beta (TGFβ) and its signaling pathways have been implicated in the initiation and progression of diverse thoracic aortopathies (Akhurst and Hata, 2012; Cook et al., 2014; Doetschman et al., 2012; Lindsay et al., 2012). For example, Loeys-Dietz syndrome (LDS) patients have a propensity for sudden aortic dissection and can be divided into one of five subtypes (LDS1, LDS2, LDS3, LDS4, and LDS5) based on the underlying gene mutations (*TGFBR1*, *TGFBR2*, *SMAD3*, *TGFB2*, and *TGFB3,* respectively) (Bertoli-Avella et al., 2015; Boileau et al., 2012; Loeys et al., 2006; Maccarrick et al., 2014; Ramirez et al., 2007; Takeda et al., 2018). In humans, the TGFβ cytokine family is comprised of three isoforms (TGFβ-1, -2, -3), each individually encoded by separate genes. Although these ligands act through a common receptor complex (TGFβR1/2), they regulate tissue development and vascular homeostasis via autocrine and/or paracrine signaling in a highly context-dependent and tissue-specific manner (Doetschman and Azhar, 2012; Moustakas and Heldin, 2009). *Tgfb1*, *Tgfb2,* and *Tgfb3* genes, for example, are expressed in a distinct yet overlapping fashion in the developing mouse aorta with *Tgfb2* and *Tgfb3* abundantly expressed in the SMCs of the medial layer and *Tgfb1* the predominant endothelial isoform (Azhar et al., 2003; Doetschman et al., 2012; Gittenberger-de Groot et al., 2006; Millan et al., 1991). Given the multifactorial nature of TGFβ there are numerous potential mechanisms through which TGFβ could affect the complex differentiation and morphogenetic processes required for healthy aortic development such as the formation of the elastic fiber network (Arthur and Bamforth, 2011).

While it is evident that appropriate TGFβ signaling is essential to vascular homeostasis, prior studies have focused predominantly on TGFβR1/2, and TGFβ-associated pathways rather than the individual ligands involved in these processes (Ferruzzi et al., 2016; Habashi et al., 2006; Holm et al., 2011; Hu et al., 2015; Li et al., 2014; Wei et al., 2017). A systematic comparison of genetic mutations in the individual TGFβ ligands and the resultant mechanical phenotypes can reveal pivotal LDS-related information. However, since knockout mouse models of TGFβ genes are lethal (Bonyadi et al., 1997; Kaartinen et al., 1995; Lindsay et al., 2012), here we examine the biaxial mechanical properties of ascending thoracic aortas (ATA) taken from heterozygous mice: *Tgfb1*$^{+/-}$, *Tgfb2*$^{+/-}$, and *Tgfb3*$^{+/-}$ and their wild-type controls. Heterozygotes were the result of germline mutations and engineered in embryonic stem cells by conventional mouse gene targeting technologies with *Tgfb2*$^{+/-}$ and *Tgfb3*$^{+/-}$ mice serving as a model for LDS4 and LDS5, respectively (Proetzel et al., 1995; Sanford et al., 1997). As a benchmark for comparison, an elastase infusion model was also used to illustrate the effects of comprehensive elastin destruction. Using sensitive biomechanical analysis techniques ATAs were studied at 4–6 months of age to glean subtle mechanical cues that could manifest as aortopathic conditions with progressive aging.

2. Methods and Materials

2.1. Animal Protocols and Genotyping

Animal protocols and euthanasia were approved through the Institutional Animal Use and Care Committee at the University of South Carolina. All mice were housed in the

Animal Research Facility at the University of South Carolina's School of Medicine. Both *Tgfb2*$^{+/-}$ and *Tgfb*3$^{+/-}$ mice were backcrossed using C57BL/6 for 12 generations and were maintained on a C57BL/6 background. Genomic DNA from mouse tails was extracted following a manufacturer's protocol (Qiagen Inc., USA). Extracted total DNA was dissolved in 100 μl of water and 1 μl was used for each PCR amplification reaction. For *Tgfb*1$^{+/-}$ mouse genotyping, we used IMF-36 (forward: 5'-AGGACCTGGGTTGGAAGTG-3'), IMR-36 (reverse: 5'-CTTCTCCGTTTCTCTGTCACCCTAT-3') and IMF-11 (neo: 5'-GCCGAGAAAGTATCCATCAT-3') primers. PCR amplification for all groups was carried out with template denaturation at 95°C for 30 sec, primers annealing at 57°C for 50 sec, and 1 min extension at 72°C with 35 cycles. PCR amplified products (216 bp for wild type and 716 for *Tgfb1* mutant alleles) were then resolved in a 1.5% agarose gel and photographed. Similarly, *Tgfb*2$^{+/-}$ mouse genotyping was carried out with the extracted tail DNA using IMF-9 (forward: 5'-AATGTGCAGGATAATTGCTGC-3') and IMR-9 (5'-AACTCCATAGATATGGGCATGC-3') primers. Wild type and *Tgfb2* heterozygous alleles were identified by the presence of 150 bp and 1.5 kb bands, respectively. For *Tgfb*3$^{+/-}$ mice the IMF-10 (forward: 5'-TGGGAGTCATGGCTGTAACT-3') and IMR-10 (reverse: 5'-CACTCACACTGGCAAGTAGT-3') primers were used. Wild type and *Tgfb3* heterozygous alleles produced 400 bp and 1.3 kb bands, respectively. All PCR reactions were performed with Econotaq plus green (Lucigen, Inc USA) using PCR machines (Eppendorf, Inc USA).

Male and female mice aged 4–6 months (*Tgfb*1$^{+/-}$, n = 4; *Tgfb*2$^{+/-}$, n = 7; *Tgfb*3$^{+/-}$, n = 6) and age-matched wild-type littermate controls (WT, n=7; elastase, n=4) underwent the complete biaxial mechanical testing protocol to be included in the final analysis. Sample sizes were based on the availability of age-matched animals from our colonies with randomization performed between littermates of WT and heterozygotes. Prior work found few sex-related differences in ATAs of wild-type mice therefore both male and female animals are included in this analysis (Ferruzzi et al., 2015). We further confirmed these findings by directly testing output variables against sex and failed to find statistical significance. Additionally, no significant differences in age-adjusted body weight were found between groups (Table 1). No other confounders were controlled for in this study. Excluded from the analysis and not included in the aforementioned sample sizes were 3 heterozygotes, 1 WT, and 3 elastase vessels that failed during surgery or cannulation (total mice used in this part of the study, N=28). All mice were euthanized via carbon dioxide inhalation and perfused through a left ventricle puncture with saline supplemented with 30 U/mL heparin sodium.

2.2. RNA isolation, cDNA synthesis, and quantitative PCR

Total RNA was isolated from ATAs taken from a separate group of *Tgfb1*$^{+/-}$ (n=3), *Tgfb2*$^{+/-}$ (n=4), *Tgfb3*$^{+/-}$ (n=4), and WT (n=3, each) mice using Trizol (Invitrogen) and miRNeasy micro kit (Qiagen) according to the manufacturer's protocols. cDNA was generated from 1μg total RNA using a Biorad RT-PCR kit according to manufacturer's instructions (Biorad) then the generated cDNA was diluted 10 times and subjected to quantitative PCR amplification (Biorad-CFX) using pre-validated *Tgfb1* (Biorad Unique Assay ID: qMmuCED0044726), *Tgfb2* (qMmuCID0024408), and *Tgfb3* (qMmuCED0045203) mouse gene-specific primers. 25 ng of cDNA was used for each 20 μl qPCR reaction.

Following qPCR analyses, the cycle count threshold (Ct) was normalized to species-specific housekeeping genes (*B2m*; Biorad Unique Assay ID: qMmuCID0040553), and the 2^-ΔCt values were determined and graphically presented.

2.3. Biomechanical Testing

After animal sacrifice, the ATA was dissected free of surrounding perivascular tissues from the aortic root to the brachiocephalic trunk. The left common carotid, subclavian artery, and distal descending aorta were ligated using 10/0 nylon suture. The ATA was then cannulated through the right innominate artery and at the aortic root using blunted 26G and 22G needles, respectively (Bellini et al., 2017; Ferruzzi et al., 2016, 2015). ATAs were mounted within our unique testing system equipped with a thin load-beam cell (Omega Engineering; LCL-113G), pressure transducer (Omega Engineering; PX409), and syringe pump all integrated and controlled via a custom LabView code and submerged within a media bath consisting of phosphate-buffered saline (PBS) (Lane et al., 2020). The axial extension ratio at which the tissue exhibits a force-pressure invariant relationship was designated the *in vivo* axial stretch ratio. This value was estimated through a series of axial-force extension tests at constant luminal pressures. Preconditioning consisted of putting arteries through five axial extension cycles from the unloaded lengths to 10% above the estimated *in vivo* stretch ratio at 40 mmHg followed by five cyclic pressurization cycles from 10–160 mmHg at the *in vivo* axial stretch ratio.

For data acquisition, all vessels except those in the elastase group were extended to three axial stretch ratios (*in vivo* ratio ± 10%) and underwent three pressurization cycles from 0–160 mmHg with simultaneous force, outer diameter, and pressure measurements at 10 mmHg increments. The elastase group was tested at a single axial stretch ratio of 1.2 that was shown to produce reliable data in preliminary examinations. We note that this value is slightly higher than those reported by Bellini et al. (2017). All data was gathered in triplicate and recorded during each loading cycle.

From the primary data collected, the mid-wall circumferential λ_θ and axial λ_z stretch ratios are calculated from

$$\lambda_\theta = \frac{r_i + r_o}{R_i + R_o}, \; \lambda_z = \frac{\ell}{L} \qquad 1$$

with R_i and R_o are the unloaded inner and outer radii respectively, r_i and r_o the deformed inner and outer radii respectively, and ℓ and L the deformed and undeformed vessel lengths, respectively.

Assuming incompressibility, the inner radii and wall thickness h for any configuration were calculated using

$$r_i = \sqrt{r_o^2 - \bar{V}/(\pi\,\ell\,)}, \; h = r_o - r_i \qquad 2$$

where $\bar{V}$ is the mean wall volume measured from 48 different deformed states using direct measurements of the inner diameter through the semi-transparent tissue. This was a necessary approach since ring samples were not possible in the wild-type group due to the elastase perfusion step in the protocol. Therefore, to maintain consistency between samples the volume was calculated from multiple deformed configurations.

The experimental mean circumferential σ_θ and axial σ_z stresses were calculated by using

$$\sigma_\theta = \frac{Pr_i}{h},\ \sigma_z = \frac{f}{\pi h(2r_i + h)} \qquad 3$$

where P is the transmural pressure and $f = F + \pi r_i^2 P$ the axial force that includes F, the force measured at the transducer, and an additional force due to pressure applied to the closed-end of the artery during inflation.

The lumen area compliance C_A was estimated from

$$C_A = \pi \frac{\Delta r_i^2}{\Delta P} \qquad 4$$

where ΔP is taken around the 100 mmHg operating point ± 10 mmHg with corresponding inner radii measurements at those loaded configurations.

2.4. Enzymatic Degradation

For the elastase-treated controls (elastase), the aorta was extended to roughly the *in vivo* stretch ratio and perfused intraluminally with 10 U/mL porcine pancreatic elastase solution. It was then pressurized to 100 mmHg for 30 minutes, followed by perfusion with Halt protease inhibitor (ThermoFisher Scientific; Cat. No. 87786) cocktail containing aprotinin. The new unloaded geometry following elastase exposure was recorded, and the vessel subsequently underwent similar testing protocols but at a single axial stretch ratio of 1.2 which was chosen due to an observed tissue instability at higher stretches.

2.5. Constitutive Modeling

Following the methodology described in greater detail in (Prim et al., 2021), we first assumed that the radial stress was relatively small so that $t_{rr} \approx 0$ and the modeled Cauchy stresses could be calculated by

$$t_{\theta\theta} = \lambda_\theta \frac{\partial W}{\partial \lambda_\theta} - \lambda_r \frac{\partial W}{\partial \lambda_r},\ t_{zz} = \lambda_z \frac{\partial W}{\partial \lambda_z} - \lambda_r \frac{\partial W}{\partial \lambda_r} \qquad 5$$

where W is the scalar-valued strain energy function. Here we employed a structurally motivated form of W using the Holzapfel-Gasser-Ogden (HGO) model that includes separate isotropic and anisotropic terms (Baek et al., 2007; Holzapfel et al., 2000)

$$W = \frac{c}{2}(I_C - 3) + \sum_{k=1}^{4} \frac{c_1^k}{4c_2^k}\left\{\exp\left[c_2^k\left(IV_C^k - 1\right)^2\right] - 1\right\} \qquad 6$$

where $I_C = \lambda_\theta^2 + \lambda_z^2 + 1/(\lambda_\theta\lambda_z)^2$, $IV_C^k = \lambda_\theta^2\sin\alpha^k + \lambda_z^2\cos\alpha^k$, and k indicates each fiber family with an angle α^k relative to the axial direction. Using this convention, the axial and circumferentially oriented fibers are given as $\alpha^1 = 0$ and $\alpha^2 = \pi/2$ respectively while $\alpha^3 = -\alpha^4$ are the symmetric and diagonal fibers. The material parameters c, c_1^k, and c_2^k are found through regression noting that for the diagonal fibers $c_1^3 = c_1^4$ and $c_2^3 = c_2^4$.

Using (5) and (6) the pressure and force can be modeled (mod) as

$$P^{\mathrm{mod}} = \frac{h}{r_i}\left[\lambda_\theta\frac{\partial W}{\partial\lambda_\theta} - \lambda_r\frac{\partial W}{\partial\lambda_r}\right],\ F^{\mathrm{mod}} = \pi h(2r_i + h)\left[2\lambda_z\frac{\partial W}{\partial\lambda_z} - \lambda_\theta\frac{\partial W}{\partial\lambda_\theta}\right] \tag{7}$$

and then best-fit parameters in (6) identified by multivariate regression analysis using a nonlinear least-squares minimization. For this, the built-in “lsqnonlin” function from MATLAB’s optimization toolbox is used to minimize the objective function

$$e = \sum_{j=1}^{n}\left[\left(\frac{P^{mod} - P^{exp}}{\overline{P}^{exp}}\right)_j^2 + \left(\frac{F^{mod} - F^{exp}}{\overline{F}^{exp}}\right)_j^2\right], \tag{8}$$

where superscript (exp) indicate experimentally measured values, respectively each with j of n observations. Pressure and force errors were normalized to their group mean values (overbars) to prevent unit-biasing and fitting errors reported as the root-mean-squared of the error (RMSE). To confirm that best-fit parameters were independent of initial guesses, six minimization cycles of random unknown parameters were generated for each initial parameter with bounds assigned so that $c > 0$, $c_1^k > 0$, $c_2^k > 0$, and $0 < \alpha < \pi/2$. Prior work using nonparametric bootstrapping revealed point-wise estimates are reliable (Ferruzzi et al., 2015; Prim et al., 2021).

Next, we utilize the theory of “small-on-large” (Baek et al., 2007) to capture appropriate linearized stiffness moduli about an operating point so that,

$$G_{\theta\theta\theta\theta} = 2\lambda_\theta\frac{\partial W}{\partial\lambda_\theta} + \lambda_\theta^2\sum_{k=1}^{4}\left(\frac{\partial^2 W^k}{\partial\lambda_\theta^2} - \frac{1}{\lambda_\theta}\frac{\partial W^k}{\partial\lambda_\theta}\right)\Bigg|_{C^\circ},\ C_{zzzz} = 2\lambda_z\frac{\partial W}{\partial\lambda_z} + \lambda_z^2\sum_{k=1}^{4}\left(\frac{\partial^2 W^k}{\partial\lambda_z^2} - \frac{1}{\lambda_z}\frac{\partial W^k}{\partial\lambda_z}\right)\Bigg|_{C^\circ}, \tag{9}$$

where $\mathbf{C}^o$ is the right Cauchy-Green deformation tensor relating the undeformed reference to the finitely deformed configuration. Linearizations and calculations of strain energy are performed around sub-physiologic, physiological, and pathological pressures of 20, 60, 100, and 140 mmHg while at *in vivo* axial stretches.

2.6. Qualitative Histology

Vessels were unloaded and placed in fresh 4% paraformaldehyde solution at 4°C overnight. Then samples were paraffin-embedded and sectioned (7 μm) for Hematoxylin and Eosin (H&E) staining and elastin autofluorescence. Transillumination light microscopy images were acquired followed by autofluorescent imaging of the same section using the EVOS FL Auto 2 microscope. For autofluorescence, a 470/22 excitation and 510/42 emission filter were used.

2.7. Statistical Analysis

Statistical analysis was performed using a two-way analysis of variance (ANOVA) with Tukey-Kramer post hoc analysis to identify differences between groups. Significant differences were identified at a level of $p<0.05$.

3. Results

Isolated mRNA from *Tgfb1*$^{+/-}$, *Tgfb2*$^{+/-}$, *Tgfb3*$^{+/-}$, and WT ATAs revealed statistically significant decreases in the expression of the corresponding *Tgfb* gene relative to the housekeeping gene (Figure 1). That is, *Tgfb1*$^{+/-}$ mice expressed *Tgfb1* at 13.1% of normal, *Tgfb2*$^{+/-}$ expressed *Tgfb2* at 41.6% of normal, and *Tgfb3*$^{+/-}$ expressed *Tgfb3* at 45.2% of the normal levels found in WT mice. Morphological assessments and biaxial mechanical testing of the ATAs reveal disparate changes in the elastase infusion model compared to wild-types with notable differences in the *Tgfb2*$^{+/-}$ group, and few differences in the *Tgfb1*$^{+/-}$ and *Tgfb3*$^{+/-}$ groups. We observed qualitatively that *Tgfb2*$^{+/-}$ mice have altered arch curvatures with a general loss of the distinct right innominate branch artery origin (Figure 2 top). *Tgfb3*$^{+/-}$ aortas also appear shorter with reduced arch curvatures. Inflation-extension patterns reinforced the changes in the elastase compared to all other groups (Figure 3) and were uniformly dilated at 100 mmHg compared to all other mice (p-val = 0.024; Figure 4). The pressure-outer diameter curve of *Tgfb1*$^{+/-}$ ATAs was shifted leftward at low pressures indicating a reduced diameter reaching statistical significance with *Tgfb3*$^{+/-}$ (p-val = 0.015) at 100 mmHg and when compared to *Tgfb2*$^{+/-}$ below 60 mmHg (p-val = 0.005) and when unloaded (p-val = 0.022; Table 1). More importantly, *Tgfb2*$^{+/-}$ mice had a statistically significant increase in loaded (p-val = 0.004) and unloaded (p-val = 0.028) wall thicknesses compared to other mice (Figure 4; Table 1).

No differences in axial force were found between groups at 100 mmHg but were present at 20 mmHg in the elastase group (p-val < 0.001) possibly due to the lower axial stretch ratio (Figure 3b). Lumen area compliance trended higher *Tgfb1*$^{+/-}$ group but large standard deviations limited the statistical findings. Circumferential stretch ratios were lower (p-val = 0.031) and circumferential (p-val < 0.001) and axial (p-val < 0.001) stresses higher in the elastase group compared to all other groups. Circumferential stresses in the *Tgfb2*$^{+/-}$ group were lower than wild-type (p-val = 0.002) and *Tgfb3*$^{+/-}$ groups (p-val = 0.021) with axial stresses in *Tgfb2*$^{+/-}$ also lower than all others (p-val < 0.001) except *Tgfb3*$^{+/-}$. Although age was found to be different between groups (p-val = 0.005), age and sex did not correlate with any of the morphological or mechanical variables studied herein.

Pressure-axial force plots illustrated the *in vivo* axial stretch ratio data with increasing force readings above, and decreasing force readings below (Figure 5). Both the resultant force and the axial stretch ratio were not statistically significant between TGFβ haploinsufficient and wild-type groups. The 1.2 axially stretch ratio of the elastase group was slightly higher than the force invariant ratio. Constitutive modeling resulted in reasonable fits to all experimental data with an average RMSE of 0.156 (Table 2). Since parameter estimation is performed through minimization of an objective function normalized by the average force and pressure measurements at various stretch states (equation 8), model limitations are indicated by an inability to reach the extremely low- and high-pressure regions of the pressure-force plot. Figure 6 illustrates the biaxial energy contour plots for TGFβ haploinsufficient and wild-type groups within the range of experimentally tested circumferential and axial stretch ratios and the approximate *in vivo* condition represented by an open circle. The elastase group was omitted from this figure due to testing at a single axial stretch ratio. Analysis of individual data points for each group taken at sub-physiologic, physiological, and pathological pressures revealed a consistent decrease in elastic energy for the *Tgfb2*$^{+/-}$ group (p-val = 0.008) and a small but significant increase in the *Tgfb1*$^{+/-}$ group (p-val < 0.017) at hypertensive pressures. *Tgfb2*$^{+/-}$ circumferential stiffnesses were generally lower than the wild-type group (p-val = 0.013) while axial stiffness was consistently lower than wild-types and *Tgfb1*$^{+/}$. Due to the 1–2 orders of magnitude greater stiffness in elastase ATAs, their data were omitted from Figure 7 but were biaxially stiffer than all other groups (p-val < 0.001) at 20 ($C_{\theta\theta\theta\theta}$ = 1.233 ± 0.422, C_{zzzz} = 6.488 ± 6.132 MPa), 60 ($C_{\theta\theta\theta\theta}$ = 3.482 ± 0.995, C_{zzzz} = 12.97 ± 11.98 MPa), 100 ($C_{\theta\theta\theta\theta}$ = 6.973 ± 2.157, C_{zzzz} = 19.76 ± 15.82 MPa), and 140 ($C_{\theta\theta\theta\theta}$ = 10.78 ± 3.155, C_{zzzz} = 25.96 ± 20.49 MPa) mmHg.

Histologically, *Tgfb1*$^{+/-}$ and for the most part *Tgfb2*$^{+/-}$ and *Tgfb3*$^{+/-}$ ATAs showed a similar microstructure to the wild-type controls while the wall thickening was apparent in the *Tgfb2*$^{+/-}$ group (Figure 8 top). Qualitatively, there were no obvious differences in smooth muscle density or orientation and the organization of non-specific extra-cellular matrix and ground substance. All aortas presented with 6–8 concentric layers of elastic lamellae interspersed with connecting fibers, but the elastin was barely perceptible in the elastase-treated ATAs. Interestingly, some *Tgfb2*$^{+/-}$ and *Tgfb3*$^{+/-}$ aortas showed signs of altered elastic structure but were not ubiquitous throughout sections (Figure 8 bottom).

4. Discussion

The differential role that TGFβ ligands play on thoracic aortopathy initiation, progression, and amelioration could be used to decipher the diversity of biomechanical phenotypes within the LDS spectrum (Bertoli-Avella et al., 2015; Boileau et al., 2012; Lindsay et al., 2012; Loeys et al., 2013, 2006; Maccarrick et al., 2014; Ramirez et al., 2007; Takeda et al., 2018). To that end, we tested the biomechanical properties of ATAs from early but mature mice with a reduction in the three primary ligands, TGFβ1, TGFβ2, and TGFβ3 due to heterozygous loss-of-function genetic mutations. Our findings revealed that only the ascending aortas from 4-to-6-month old *Tgfb2*$^{+/-}$ mice had a significant biomechanical phenotype while, for the most part, those taken from *Tgfb1*$^{+/-}$ and *Tgfb3*$^{+/-}$ mice revealed little-to no deviation from WT controls. Furthermore, the TGFβ ligand models did not possess the severe aortopathic features present in the elastase treated model.

Tgfb2$^{+/-}$ ATAs showed significantly increased wall thickness, decreased biaxial states of stress, a reduction in stored energy, and a reduction in most measures of biaxial stiffness. These findings were largely in agreement with earlier work using the same animal model but with a different mechanical testing device (Keyes et al., 2010). In contrast, aneurysm-types of aortopathy typically present with dilation, wall-thinning, and increased stiffness such as that shown by matrix destruction found in the elastase group (Collins et al., 2012; Lane et al., 2020). Overall, it remains unclear what factors drive *Tgfb2*$^{+/-}$ wall thickening without dilation but compensatory TGFβ signaling and altered mechanosensing could be driving maladaptive remodeling (Humphrey et al., 2014; Milewicz et al., 2017; Pannu et al., 2007). More advanced gene expression and microscopy techniques would be needed to decipher these subtle changes.

Conventional *in vivo* assessment of aneurysm formation typically involves ultrasound studies relying on direct measures of inner diameter while many *ex vivo* studies largely focus on excised ring segments in uniaxial extension. In the current investigation, we used biaxial testing to report on additional metrics including the outer radius, wall thickness, and axial force as well as the biaxial state of stress, stretch, and stiffness. Still, our findings were consistent with those of Grainger et al. that suggest an absence of aortic disease in young *Tgfb1*$^{+/-}$ mice (Grainger et al., 2000). In contrast, Lindsay et al. found that the aortic root of *Tgfb2*$^{+/-}$ mice trended towards dilation at 4 months of age and reached significant dilation and aneurysm classification at 8 months (Lindsay et al., 2012). Since a comprehensive biomechanical analysis of the aortic root is difficult, we anticipated that the underlying connective tissue abnormalities would be detectable in the ascending aorta of *Tgfb2*$^{+/-}$ mice as early as 4–6 months. It remains to be seen if aortic aneurysms develop in these groups with advanced aging.

Although we did not measure blood pressure directly in our study, Lindsay et al., (2012) and separately Zacharias et al., (2004) failed to find statistical significance between *Tgfb1*$^{+/-}$ or *Tgfb2*$^{+/-}$ mice and their wild-type littermates. Thus, to facilitate comparisons between groups, discrete pressures were selected based on the anticipated relative contribution of different constituents to the overall mechanical behavior around that operating point with highly undulated collagen engaged at higher stretches (Roach and Burton, 1957). Interestingly, *Tgfb1*$^{+/-}$ aortas had a reduced diameter in low-stretch portions of the distensibility curve (< 100 mmHg) typically dominated by elastin. We also observed a trend towards higher luminal compliance in *Tgfb1*$^{+/-}$ ATAs but failing to reach statistical significance. Despite the low sample size used for this group, measures of luminal compliance typically have large standard deviations (Prim et al., 2018). On the other hand, excised *Tgfb3*$^{+/-}$ aortas revealed few morphological changes qualitatively observed upon gross dissection. Our prior work reported that *Tgfb3*$^{-/-}$ mouse embryos exhibit abnormalities in the vascular walls of both the aorta and pulmonary trunk (Chakrabarti et al., 2020). Despite this, *Tgfb3*$^{+/-}$ aortas studied herein did not reach statistical significance in most biomechanical categories. Our current study, however, assumes long cylindrical segments and was focused on the ascending portion of the thoracic aorta and not the arch that may contribute to these discrepancies.

TGFβ signaling is a complex and multifaceted process. Paradoxically, both enhanced TGFβ signaling and loss of function TGFBR (receptor) mutations are involved in the initiation and progression of thoracic aortopathies (Hu et al., 2015). The individual TGFβ1, TGFβ2, and TGFβ3 ligands all signal through a common TGFβ receptor complex with mutations in TGFβ receptors and their pathways integral to LDS-related aortopathies (Boileau et al., 2012; Doyle et al., 2012; Isselbacher et al., 2016). Our observed increases in wall thickness and decreases in energy storage found in the *Tgfb2*$^{+/-}$ were similar to those using *Tgfbr2* conditional inactivation that eventually leads to progressive aortic dilation, wall thickening, and dissection (Ferruzzi et al., 2016; Li et al., 2014). An important consideration in the use of our heterozygous loss-of-function models is the compensatory biological signaling of TGFβ ligands during development that can be up and down-regulated in response to a reduction in one specific ligand. Future studies will need to quantify how gene and protein expression of the other ligand isoforms are modulated. For now, we consider the unquantified regulation of the alternate ligands a limitation in our approach. Likewise, the mechanical properties of our aortas were studied in a passivated state so that properties of the extra-cellular matrix remained the focus of the current investigation and smooth muscle contractility was not assessed. Many studies have also shown that these smooth muscle contractile proteins are targets of TGFβ signaling suggesting that they may be responsible for transducing changes in TGFβ signals that affect altered contractility (Guo and Chen, 2012; Loeys et al., 2006).

Our study was performed in an age group targeting a post-developmental but “pre-aneurysmal” state to identify biomechanical features not easily discerned using traditional *in vivo* techniques. In connective tissue disorders such as LDS, the lethal sequelae of sudden-onset dissection and rupture events may already be initiated by the time it is detected using ultrasound screening - if detected at all. Therefore, understanding the timeline of events and the subtle clues presented by thoracic aortopathy are crucial to making improvements in preemptive therapeutic interventions. Both male and female mice were used in the current study. Although sex was not found to correlate with any of our output variables, additional samples would be necessary to decipher the role of age and sex in LDS-related aortopathies. The current work is the first of its kind to present a unified approach to studying the biaxial properties from the ascending aortas of mice with a heterozygous loss-of-function mutation of the individual TGFβ isoform genes, namely *Tgfb1*$^{+/-}$, *Tgfb2*$^{+/-}$, and *Tgfb3*$^{+/-}$ genotypes, and their controls, there remains a need to link these findings to the lethal aspect of LDS-related aortopathies.

Acknowledgments

The authors would like to acknowledge the contributions of John Johnson and Aniket Bhattacharya for their assistance in animal genotyping, animal care, and dissection and Shahd Hasanain, Liya Du, and Nazli Gharraee for their assistance in data collection and processing. This work was supported through funding from the American Heart Association (17GRNT33650018) and by the National Institutes of Health under grants number (R01HL133662, R01HL145064, R01HL126705).

5. References

Akhurst RJ, Hata A, 2012. Targeting the TGFbeta signalling pathway in disease. Nat. Rev. Drug Discov11, 790–811. [PubMed: 23000686]

Arthur HM, Bamforth SD, 2011. TGFbeta signaling and congenital heart disease: Insights from mouse studies. Birth Defects Res. A Clin. Mol. Teratol91, 423–434. [PubMed: 21538815]

Azhar M, Schultz JEJ, Grupp I, Dorn GW, Meneton P, Molin DGM, Gittenberger-de Groot AC, Doetschman T, 2003. Transforming growth factor beta in cardiovascular development and function. Cytokine Growth Factor Rev. 14, 391–407. [PubMed: 12948523]

Baek S, Gleason RL, Rajagopal KR, Humphrey JD, 2007. Theory of small on large: potential utility in computations of fluid–solid interactions in arteries. Comput. Methods Appl. Mech. Eng196, 3070–3078.

Bellini C, Bersi MR, Caulk AW, Ferruzzi J, Milewicz DM, Ramirez F, Rifkin DB, Tellides G, Yanagisawa H, Humphrey JD, 2017. Comparison of 10 murine models reveals a distinct biomechanical phenotype in thoracic aortic aneurysms. J. R. Soc. Interface14, 20161036. 10.1098/rsif.2016.1036 [PubMed: 28490606]

Bertoli-Avella AM, Gillis E, Morisaki H, Verhagen JMA, de Graaf BM, van de Beek G, Gallo E, Kruithof BPT, Venselaar H, Myers LA, Laga S, Doyle AJ, Oswald G, van Cappellen GWA, Yamanaka I, van der Helm RM, Beverloo B, de Klein A, Pardo L, Lammens M, Evers C, Devriendt K, Dumoulein M, Timmermans J, Bruggenwirth HT, Verheijen F, Rodrigus I, Baynam G, Kempers M, Saenen J, Van Craenenbroeck EM, Minatoya K, Matsukawa R, Tsukube T, Kubo N, Hofstra R, Goumans MJ, Bekkers JA, Roos-Hesselink JW, van de Laar IMBH, Dietz HC, Van Laer L, Morisaki T, Wessels MW, Loeys BL, 2015. Mutations in a TGF-β Ligand, TGFB3, Cause Syndromic Aortic Aneurysms and Dissections. J. Am. Coll. Cardiol. 65, 1324–1336. 10.1016/j.jacc.2015.01.040 [PubMed: 25835445]

Boileau C, Guo DC, Hanna N, Regalado ES, Detaint D, Gong L, Varret M, Prakash SK, Li AH, d'Indy H, Braverman AC, Grandchamp B, Kwartler CS, Gouya L, Santos-Cortez RL, Abifadel M, Leal SM, Muti C, Shendure J, Gross MS, Rieder MJ, Vahanian A, Nickerson DA, Michel JB, Jondeau G, Milewicz DM, 2012. TGFB2 mutations cause familial thoracic aortic aneurysms and dissections associated with mild systemic features of Marfan syndrome. Nat. Genet44, 916–921. [PubMed: 22772371]

Bonyadi M, Rusholme SAB, Cousins FM, Su HC, Biron CA, Farrall M, Akhurst RJ, 1997. Mapping of a major genetic modifier of embryonic lethality in TGFβ1 knockout mice. Nat. Genet. 15, 207–211. 10.1038/ng0297-207 [PubMed: 9020852]

Chakrabarti M, Al-Sammarraie N, Gebere MG, Bhattacharya A, Chopra S, Johnson J, Peña EA, Eberth JF, Poelmann RE, Gittenberger-de Groot AC, Azhar M, 2020. Transforming Growth Factor Beta3 is Required for Cardiovascular Development. J. Cardiovasc. Dev. Dis7, 19. 10.3390/jcdd7020019

Collins MJ, Eberth JF, Wilson E, Humphrey JD, 2012. Acute mechanical effects of elastase on the infrarenal mouse aorta: implications for models of aneurysms. J. Biomech45, 660–5. 10.1016/j.jbiomech.2011.12.013 [PubMed: 22236532]

Cook JR, Carta L, Galatioto J, Ramirez F, 2014. Cardiovascular manifestations in Marfan syndrome and related diseases; multiple genes causing similar phenotypes. Clin. Genet10.

Doetschman T, Azhar M, 2012. Cardiac-specific inducible and conditional gene targeting in mice. Circ. Res110, 1498–1512. [PubMed: 22628574]

Doetschman T, Barnett JV, Runyan RB, Camenisch TD, Heimark RL, Granzier HL, Conway SJ, Azhar M, 2012. Transforming growth factor beta signaling in adult cardiovascular diseases and repair. Cell Tissue Res347, 203–223. [PubMed: 21953136]

Doyle AJ, Doyle JJ, Bessling SL, Maragh S, Lindsay ME, Schepers D, Gillis E, Mortier G, Homfray T, Sauls K, Norris RA, Huso ND, Leahy D, Mohr DW, Caulfield MJ, Scott AF, Destree A, Hennekam RC, Arn PH, Curry CJ, van LL, McCallion AS, Loeys BL, Dietz HC, 2012. Mutations in the TGF-beta repressor SKI cause Shprintzen-Goldberg syndrome with aortic aneurysm. Nat. Genet10.

Ferruzzi J, Bersi MR, Uman S, Yanagisawa H, Humphrey JD, 2015. Decreased Elastic Energy Storage, Not Increased Material Stiffness, Characterizes Central Artery Dysfunction in Fibulin-5 Deficiency Independent of Sex. J. Biomech. Eng. 137, 1–14. 10.1115/1.4029431

Ferruzzi J, Murtada S. Il, Li G, Jiao Y, Uman S, Ting MYL, Tellides G, Humphrey JD, 2016. Pharmacologically improved contractility protects against aortic dissection in mice with disrupted transforming growth factor-β signaling despite compromised extracellular matrix properties. Arterioscler. Thromb. Vasc. Biol36, 919–927. 10.1161/ATVBAHA.116.307436 [PubMed: 26988590]

Gittenberger-de Groot AC, Azhar M, Molin DG, 2006. Transforming growth factor beta-SMAD2 signaling and aortic arch development. Trends Cardiovasc. Med16, 1–6. [PubMed: 16387623]

Grainger DJ, Mosedale DE, Metcalfe JC, Bottinger EP, 2000. Dietary fat and reduced levels of TGFbeta1 act synergistically to promote activation of the vascular endothelium and formation of lipid lesions. J. Cell Sci. 113, 2355 LP–2361. [PubMed: 10852815]

Guo X, Chen SY, 2012. Transforming growth factor-beta and smooth muscle differentiation. World J. Biol. Chem3, 41–52. [PubMed: 22451850]

Habashi JP, Judge DP, Holm TM, Cohn RD, Loeys BL, Cooper TK, Myers L, Klein EC, Liu G, Calvi C, Podowski M, Neptune ER, Halushka MK, Bedja D, Gabrielson K, Rifkin DB, Carta L, Ramirez F, Huso DL, Dietz HC, 2006. Losartan, an AT1 antagonist, prevents aortic aneurysm in a mouse model of Marfan syndrome. Science (80-.). 312, 117–121.

Holm TM, Habashi JP, Doyle JJ, Bedja D, Chen Y, van Erp C, Lindsay ME, Kim D, Schoenhoff F, Cohn RD, Loeys BL, Thomas CJ, Patnaik S, Marugan JJ, Judge DP, Dietz HC, 2011. Noncanonical TGF Signaling Contributes to Aortic Aneurysm Progression in Marfan Syndrome Mice. Science (80-.). 10.1126/science.1192149

Holzapfel GA, Gasser TC, Ogden RW, 2000. A New Constitutive Framework for Arterial Wall Mechanics and a Comparative Study of Material Models. J. Elast. Phys. Sci. solids61, 1–48. 10.1023/A:1010835316564

Hu JH, Wei H, Jaffe M, Airhart N, Du L, Angelov SN, Yan J, Allen JK, Kang I, Wight TN, Fox K, Smith A, Enstrom R, Dichek DA, 2015. Postnatal Deletion of the Type II Transforming Growth Factor-beta Receptor in Smooth Muscle Cells Causes Severe Aortopathy in Mice. Arter. Thromb Vasc Biol35, 2647–2656. 10.1161/ATVBAHA.115.306573

Humphrey JD, Milewicz DM, Tellides G, Schwartz MA, 2014. Dysfunctional Mechanosensing in Aneurysms. Science (80-.). 344, 477 LP–479.

Isselbacher EM, Lino Cardenas CL, Lindsay ME, 2016. Hereditary Influence in Thoracic Aortic Aneurysm and Dissection. Circulation133, 2516–2528. 10.1161/CIRCULATIONAHA.116.009762 [PubMed: 27297344]

Kaartinen V, Voncken JW, Shuler C, Warburton D, Bu D, Heisterkamp N, Groffen J, 1995. Abnormal lung development and cleft palate in mice lacking TGF–β3 indicates defects of epithelial–mesenchymal interaction. Nat. Genet11, 415–421. 10.1038/ng1295-415 [PubMed: 7493022]

Keyes JT, Borowicz S, Utzinger U, Azhar M, Vande Geest JP, 2010. Quantification of the biomechanical differences in wild-type and heterozygous TGF beta2 knockout mice, in: ASME 2010 Summer Bioengineering Conference, SBC 2010. Naples, Florida, USA, pp. 721–722. 10.1115/SBC2010-19482

Lane BA, Wang X, Lessner SM, Vyavahare NR, Eberth JF, 2020. Targeted Gold Nanoparticles as an Indicator of Mechanical Damage in an Elastase Model of Aortic Aneurysm. Ann. Biomed. Eng48, 2268–2278. 10.1007/s10439-020-02500-5 [PubMed: 32240423]

Li W, Li Q, Jiao Y, Qin L, Ali R, Zhou J, Ferruzzi J, Kim RW, Geirsson A, Dietz HC, Offermanns S, Humphrey JD, Tellides G, 2014. Tgfbr2 disruption in postnatal smooth muscle impairs aortic wall homeostasis. J. Clin. Invest124, 755–767. [PubMed: 24401272]

Lindsay ME, Schepers D, Bolar NA, Doyle JJ, Gallo E, Fert-Bober J, Kempers MJE, Fishman EK, Chen Y, Myers L, Bjeda D, Oswald G, Elias AF, Levy HP, Anderlid B-MM, Yang MH, Bongers EMHF, Timmermans J, Braverman AC, Canham N, Mortier GR, Brunner HG, Byers PH, Van EJ, van LL, Dietz HC, Loeys BL, Van Eyk J, Van Laer L, Dietz HC, Loeys BL, Van EJ, van LL, Dietz HC, Loeys BL, 2012. Loss-of-function mutations in TGFB2 cause a syndromic presentation of thoracic aortic aneurysm. Nat. Genet44, 922–927. 10.1038/ng.2349 [PubMed: 22772368]

Loeys BL, Mortier G, Dietz HC, 2013. Bone lessons from Marfan syndrome and related disorders: fibrillin, TGF-B and BMP at the balance of too long and too short. Pediatr. Endocrinol. Rev10 Suppl 2, 417–423. [PubMed: 23858625]

Loeys BL, Schwarze U, Holm T, Callewaert BL, Thomas GH, Pannu H, De Backer JF, Oswald GL, Symoens S, Manouvrier S, Roberts AE, Faravelli F, Greco MA, Pyeritz RE, Milewicz DM, Coucke PJ, Cameron DE, Braverman AC, Byers PH, De Paepe AM, Dietz HC, 2006. Aneurysm syndromes caused by mutations in the TGF-beta receptor. N. Engl. J. Med355, 788–798. [PubMed: 16928994]

Maccarrick G, Black JH III, Bowdin S, El-Hamamsy I, Frischmeyer-Guerrerio PA, Guerrerio AL, Sponseller PD, Loeys B, Dietz HC III, 2014. Loeys-Dietz syndrome: a primer for diagnosis and management. Genet. Med10.

Milewicz DM, Trybus KM, Guo DC, Sweeney HL, Regalado E, Kamm K, Stull JT, 2017. Altered smooth muscle cell force generation as a driver of thoracic aortic aneurysms and dissections. Arterioscler. Thromb. Vasc. Biol37, 26–34. 10.1161/ATVBAHA.116.303229 [PubMed: 27879251]

Millan FA, Denhez F, Kondaiah P, Akhurst RJ, 1991. Embryonic gene expression patterns of TGF beta 1, beta 2 and beta 3 suggest different developmental functions in vivo. Development111, 131–143. [PubMed: 1707784]

Moustakas A, Heldin CH, 2009. The regulation of TGFbeta signal transduction. Development136, 3699–3714. [PubMed: 19855013]

Pannu H, Tran-Fadulu V, Papke CL, Scherer S, Liu Y, Presley C, Guo D, Estrera AL, Safi HJ, Brasier AR, Vick GW, Marian AJ, Raman CS, Buja LM, Milewicz DM, 2007. MYH11 mutations result in a distinct vascular pathology driven by insulin-like growth factor 1 and angiotensin II. Hum. Mol. Genet16, 2453–2462. [PubMed: 17666408]

Prim DA, Lane BA, Ferruzzi J, Shazly T, Eberth JF, 2021. Evaluation of the Stress–Growth Hypothesis in Saphenous Vein Perfusion Culture. Ann. Biomed. Eng49, 487–501. 10.1007/s10439-020-02582-1 [PubMed: 32728831]

Prim DA, Mohamed MA, Lane BA, Poblete K, Wierzbicki MA, Lessner SM, Shazly T, Eberth JF, 2018. Comparative mechanics of diverse mammalian carotid arteries. PLoS One13, e0202123. [PubMed: 30096185]

Proetzel G, Pawlowski SA, Wiles MV, Yin M, Boivin GP, Howles PN, Ding J, Ferguson MWJ, Doetschman T, 1995. Transforming growth factor–β3 is required for secondary palate fusion. Nat. Genet11, 409–414. 10.1038/ng1295-409 [PubMed: 7493021]

Ramirez F, Sakai LY, Rifkin DB, Dietz HC, 2007. Extracellular microfibrils in development and disease. Cell Mol. Life Sci64, 2437–2446. [PubMed: 17585369]

Roach M, Burton C, 1957. The Reason for the Shape of the Distensibility of Curves of Arteries. Can. J. Biochem. Physiol

Sanford LP, Ormsby I, Gittenberger-de GAC, Sariola H, Friedman R, Boivin GP, Cardell EL, Doetschman T, 1997. TGFbeta2 knockout mice have multiple developmental defects that are non-overlapping with other TGFbeta knockout phenotypes. Development124, 2659–2670. [PubMed: 9217007]

Takeda N, Hara H, Fujiwara T, Kanaya T, Maemura S, Komuro I, 2018. TGF-β signaling-related genes and thoracic aortic aneurysms and dissections. Int. J. Mol. Sci19. 10.3390/ijms19072125

Wei H, Hu JH, Angelov SN, Fox K, Yan J, Enstrom R, Smith A, Dichek DA, 2017. Aortopathy in a Mouse Model of Marfan Syndrome Is Not Mediated by Altered Transforming Growth Factor β Signaling. J. Am. Heart Assoc10.1161/JAHA.116.004968

Zacharias A, Habib RH, Schwann TA, Riordan CJ, Durham SJ, Shah A, 2004. Improved Survival With Radial Artery Versus Vein Conduits in Coronary Bypass Surgery With Left Internal Thoracic Artery to Left Anterior Descending Artery Grafting. Circulation109, 1489–1496. [PubMed: 15023868]

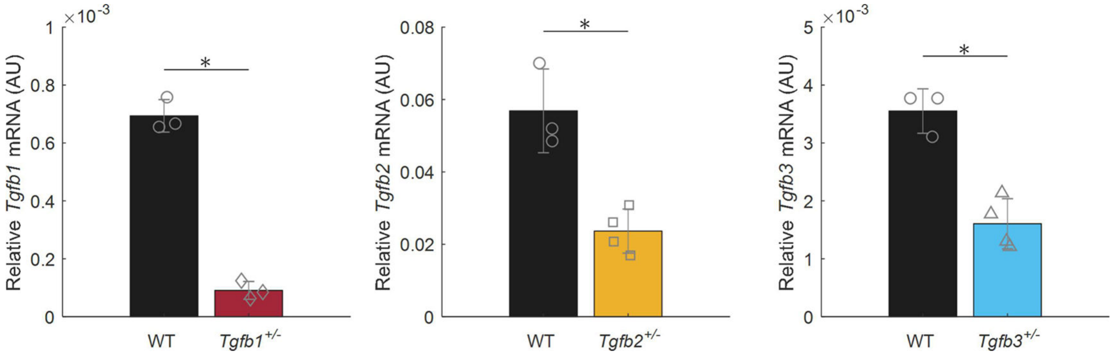

Figure 1.

Tgfb1, *Tgfb*2, and *Tgfb*3 mRNA expression in ascending thoracic aortas taken from *Tgfb1*$^{+/-}$ (n=3), *Tgfb2*$^{+/-}$ (n=4), and *Tgfb3*$^{+/-}$ (n=4), mice and their wild-type (WT) controls (n=3 each). All expression levels are relative to the *B2m* housekeeping gene. * Denotes statistical significance between heterozygotes and their WT controls at $p<0.05$.

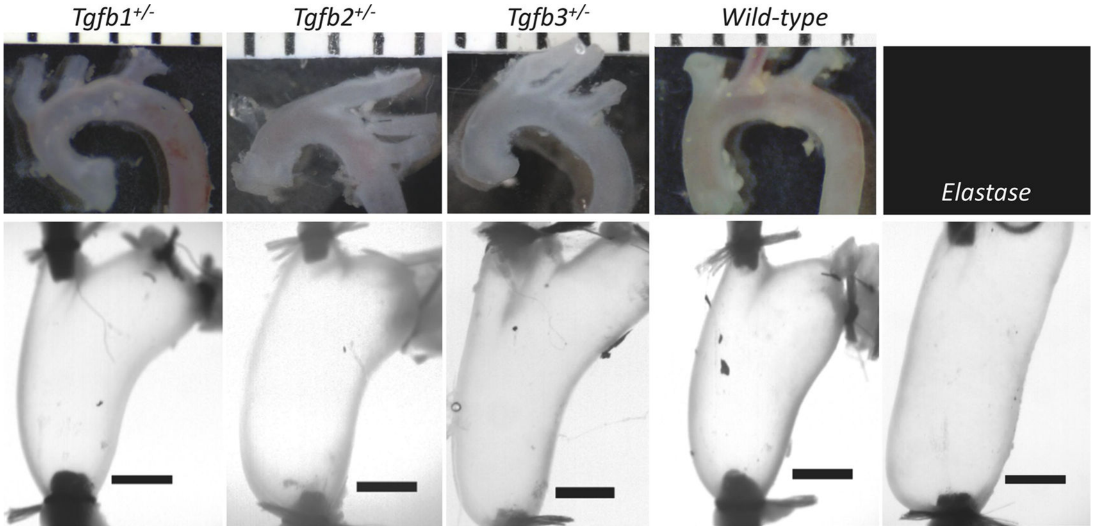

Figure 2.

Representative images of the ascending thoracic aortas from *Tgfb1*$^{+/-}$, *Tgfb*2$^{+/-}$, *Tgfb*3$^{+/-}$, wild-type, and Elastase infused wild-type mice prior to, (top) and following cannulation, axial extension, and pressurization to 100 mmHg (bottom). (top) Ruler with mm units and (bottom) 1 mm scale bars. Elastase infusion is performed in the loaded configuration.

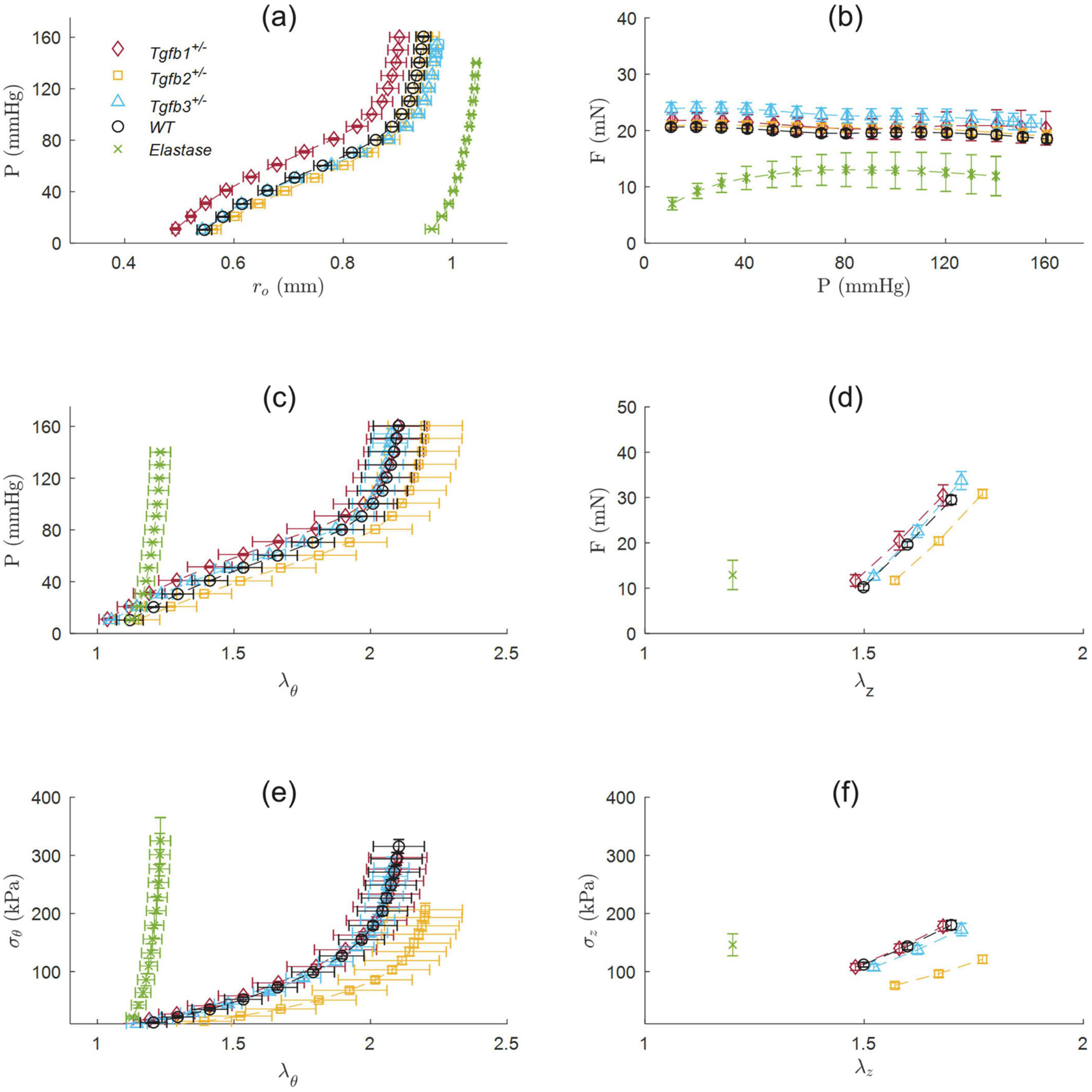

Figure 3.

Biaxial mechanical data from the ascending aortas of *Tgfb1*$^{+/-}$ (red diamonds), *Tgfb2*$^{+/-}$ (yellow squares), *Tgfb3*$^{+/-}$ (blue triangles), wild-type (WT; black circles), and elastase infused wild-type (Elastase; green X) mice. As a subset of the total biaxial mechanical data, (a-c,e) are reported at a single axial stretch ratio and (d,f) at a single pressure of 100 mmHg. Experimental data are shown as mean values ± the standard error of the mean.

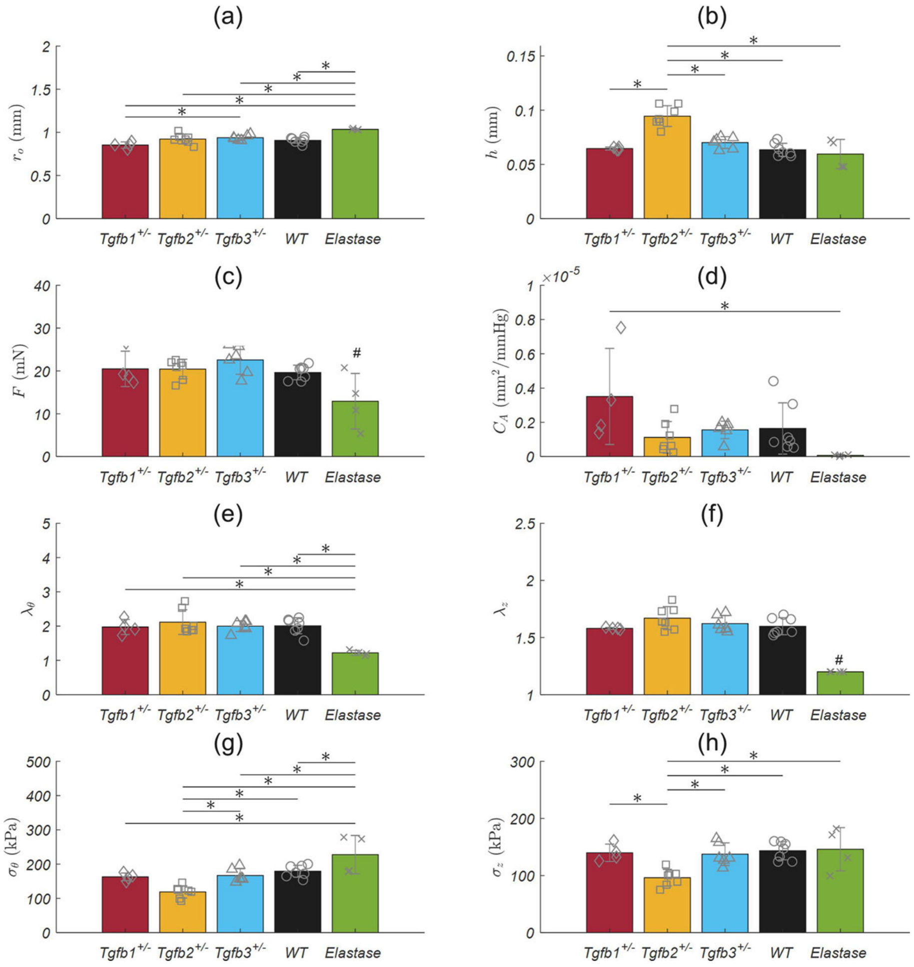

Figure 4.

Passive structural and mechanical properties from the ascending aortas of *Tgfb1*$^{+/-}$ (red), *Tgfb2*$^{+/-}$ (yellow), *Tgfb3*$^{+/-}$ (blue), wild-type (WT; black), and elastase infused wild-type (Elastase; green) mice. All values are mean ± standard deviation. * Denotes statistical significance between groups at $p<0.05$ while ** simplifies statistical significance between the elastase and all other groups. # Elastase samples were tested at a single axial stretch ratio.

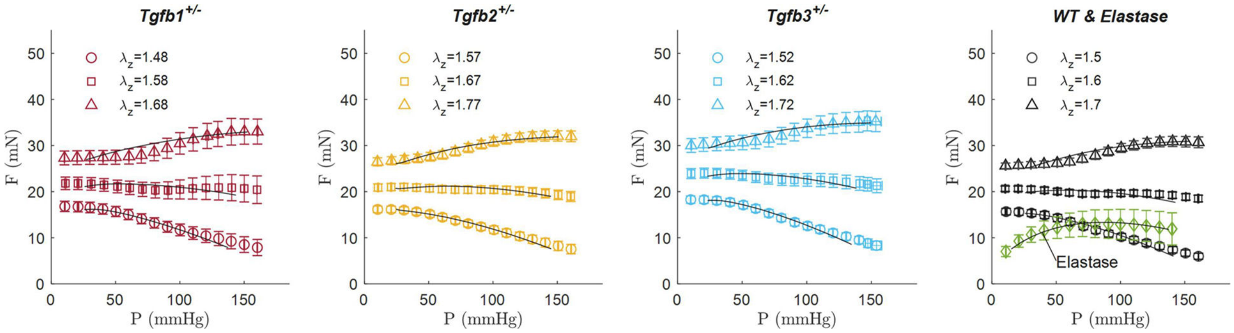

Figure 5.

Averaged and fitted pressure-force data taken from the ascending aortas of *Tgfb1*$^{+/-}$, *Tgfb2*$^{+/-}$, *Tgfb3*$^{+/-}$, wild-type (WT), and elastase infused wild-type (Elastase) mice. Experimental data are shown as discrete values ± the standard error of the mean at low (blue circle), medium (red square), and high (yellow triangle) axial stretch ratios. The medium condition represents the force-invariant pressurization axial stretch ratio. Fitted results using the 4-fiber-family Holzapfel-Gasser-Ogden (HGO) model are represented by curves (black). The elastase sample (green diamond) was tested at a single axial stretch ratio.

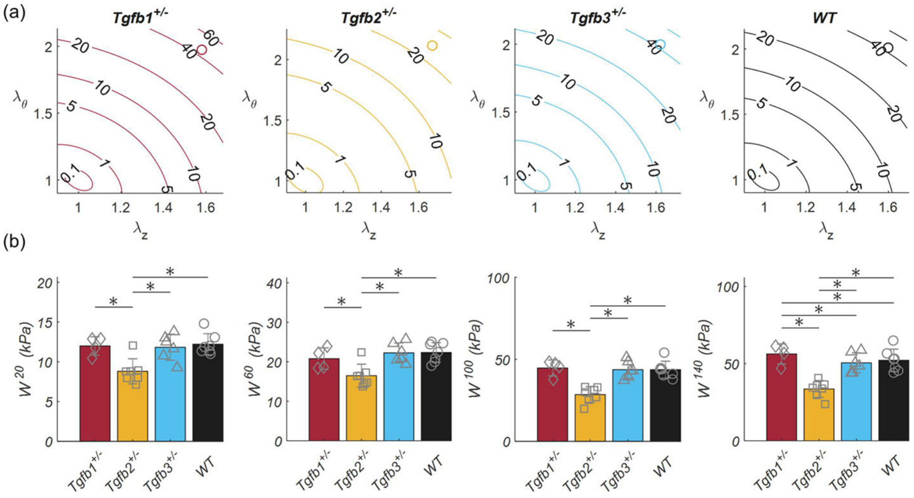

Figure 6.

Stored elastic energy of ascending aortas shown as (top) contour plots with open circles at in vivo conditions and (bottom) discrete values of stored energy taken at 20, 60, 100, and 140 mmHg taken from *Tgfb1*$^{+/-}$ (red), *Tgfb2*$^{+/-}$ (yellow), *Tgfb3*$^{+/-}$ (blue) and (d) wild-type (WT; black) mice. * Denotes statistical significance between groups at $p<0.05$.

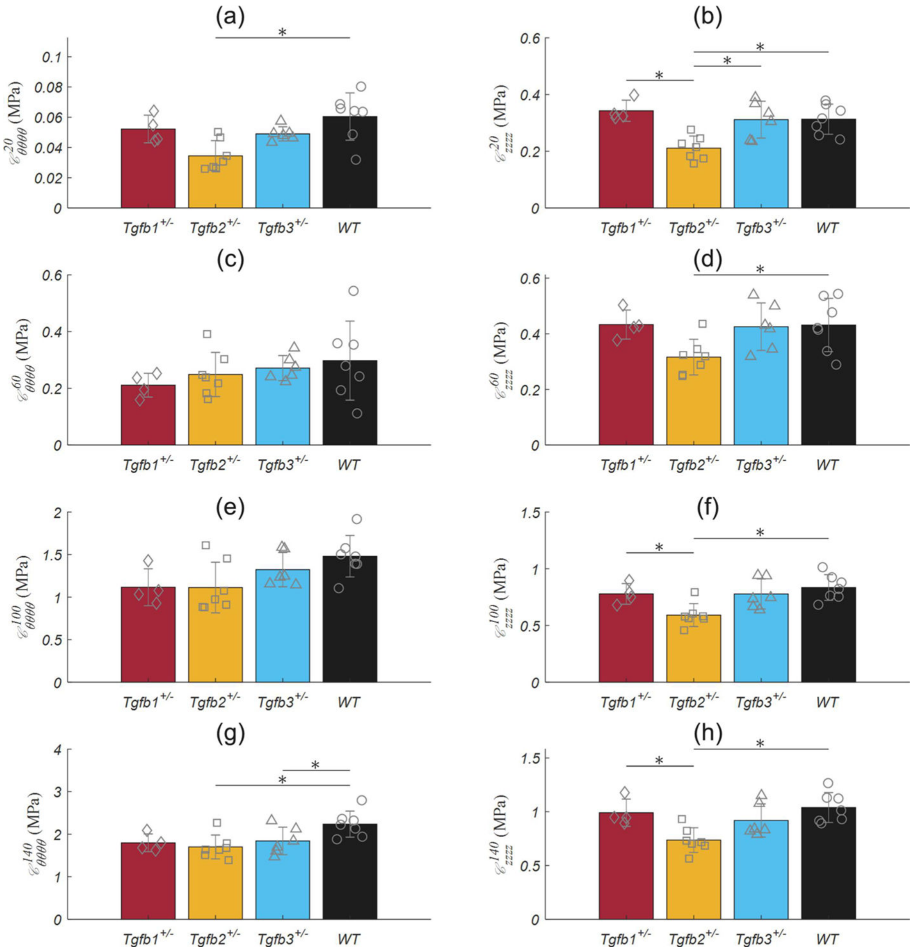

Figure 7.

Ascending aortic (left) circumferential and (right) axial stiffness moduli from *Tgfb1*$^{+/-}$ (red), *Tgfb2*$^{+/-}$ (yellow), *Tgfb3*$^{+/-}$ (blue), and wild-type (WT; black) mice. Linearizations were performed around conditions corresponding to force-invariant axial stretch and (a) 20, (b) 60, (c) 100, and (d) 140 mmHg. * Denotes statistical significance between individual groups at $p<0.05$. conditions.

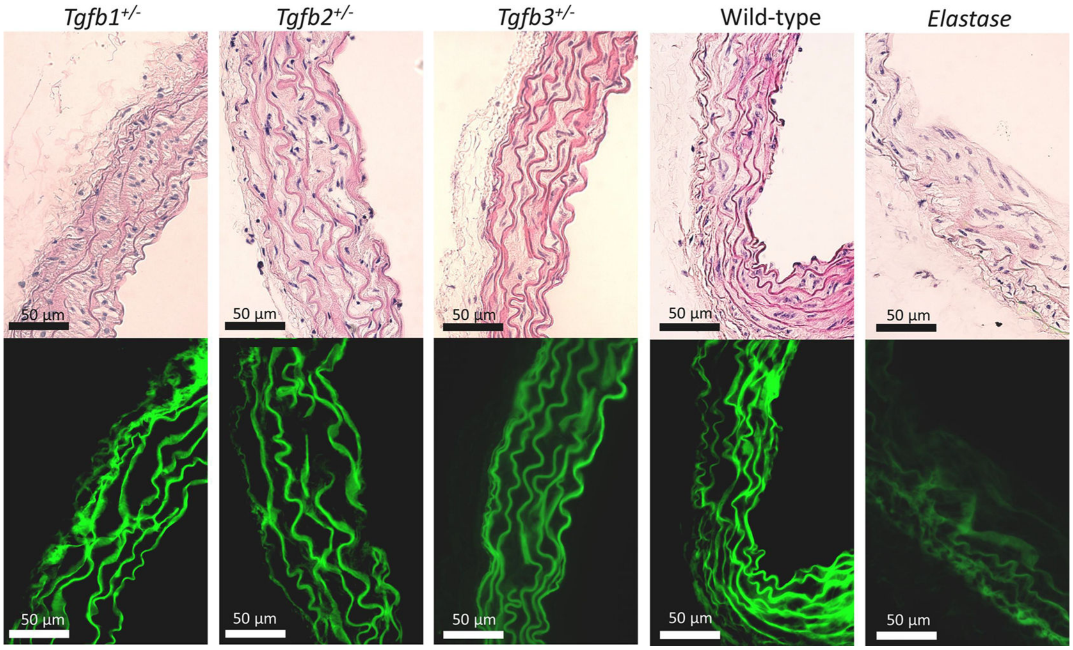

Figure 8.

Histological features using (top) Hematoxylin and Eosin staining and (bottom) elastin autofluorescence of the ascending aortas taken from *Tgfb1*$^{+/-}$, *Tgfb2*$^{+/-}$, *Tgfb3*$^{+/-}$, wild-type (WT), and elastase infused wild-type (Elastase) mice. All images at 40x.

Table 1.

Mouse age at sacrifice, body weight, and unloaded outer radii of ascending aortas (ATA) taken from *Tgfb1*$^{+/-}$, *Tgfb2*$^{+/-}$, *Tgfb3*$^{+/-}$, wild-type (WT), and elastase infused (Elastase) wild-type mice.

	Tgfb1 $^{+/-}$	***Tgfb2*** $^{+/-}$	***Tgfb3*** $^{+/-}$	**WT**	**Elastase**
Age (months)	$4.25 \pm 0.5^{\S}$	$5.71 \pm 0.76^{\wedge}$	$4.0 \pm 0.0^{\S}$	5.25 ± 1.0	4.92 ± 0.37
Body Weight (grams)	31.2 ± 5.20	30.1 ± 1.80	27.1 ± 3.15	29.0 ± 3.82	-
Unloaded Outer Radius (μm)	$518.2 \pm 18.2^{\S\wedge}$	$591.3 \pm 33.62^{\wedge}$	$566.4 \pm 29.6^{\wedge}$	$524.2 \pm 22.2^{\wedge}$	$869.9 \pm 51.9^{*}$

§, *, and ^ indicate statistical significance of groups with *Tgfb2*$^{+/-}$ wild-type, or elastase mice, respectively.

Table 2.

Pointwise best fit material parameters for *Tgfb1*$^{+/-}$, *Tgfb2*$^{+/-}$, *Tgfb3*$^{+/-}$, WT, and elastase ATAs using the 4-fiber-family Holzapfel-Gasser-Ogden (HGO) model with averaged data.

	Isotropic	**Axial Fibers**		**Circ. Fibers**		**Diagonal Fibers**			**Error**
	c (kPa)	**c_1^1 (kPa)**	**c_2^1**	**c_1^2 (kPa)**	**c_2^2**	**$c_1^{3,4}$ (kPa)**	**$c_2^{3,4}$**	**α (rad)**	**RMSE**
Tgfb1 $^{+/-}$	7.200	10.41	0.003	1.816	1.35×10^{-6}	5.337	0.233	0.761	0.200
Tgfb2 $^{+/-}$	4.349	4.956	0.022	0.027	0.071	1.377	0.257	0.807	0.167
Tgfb3 $^{+/-}$	8.317	7.193	0.002	0.967	1.01×10^{-6}	3.950	0.278	0.821	0.181
WT	7.825	8.233	0.009	0.285	0.043	3.939	0.267	0.794	0.196
Elastase	1.489	3.315	6.277	14.68	10.28	2.882	19.48	0.705	0.039